



HAL
open science

Design method of PCB inductors for high-frequency GaN converters

Ammar Chafi, Nadir Idir, Arnaud Videt, Hassan Maher

► **To cite this version:**

Ammar Chafi, Nadir Idir, Arnaud Videt, Hassan Maher. Design method of PCB inductors for high-frequency GaN converters. *IEEE Transactions on Power Electronics*, 2020, 36 (1), pp.805 - 814. 10.1109/TPEL.2020.3000438 . hal-03830532

HAL Id: hal-03830532

<https://hal.univ-lille.fr/hal-03830532v1>

Submitted on 26 Oct 2022

HAL is a multi-disciplinary open access archive for the deposit and dissemination of scientific research documents, whether they are published or not. The documents may come from teaching and research institutions in France or abroad, or from public or private research centers.

L'archive ouverte pluridisciplinaire **HAL**, est destinée au dépôt et à la diffusion de documents scientifiques de niveau recherche, publiés ou non, émanant des établissements d'enseignement et de recherche français ou étrangers, des laboratoires publics ou privés.

Design method of PCB inductors for high-frequency GaN converters

Ammar Chafi, Nadir Idir, *Member, IEEE*, Arnaud Videt, *Member, IEEE*, and Hassan Maher, *Member, IEEE*

Abstract—The new power GaN transistors allow to increase the operating frequency of converters to megahertz range, thanks to their low switching time that is of a few nanoseconds or less. This permits to reduce the values and the volume of the passive components, and enhance the power density of power converters. However, inductors needed for energy storage still take a large volume in converters compared with the others components, because of their weak energy density. Further, high-frequency operation require low-losses magnetic materials. In this paper, a design method of PCB inductors is proposed. A flexible ferrite sheet is used to enhance the inductance value and ease the realization of custom-shape devices. The design method of the inductor is based on the optimization of the inductor volume taking into account thermal issues of the magnetic sheets. Also a simulation method is proposed to calculate the equivalent stray capacitance of the inductors. The proposed method provides a losses-volume trade-off that helps designers to optimize the inductor for their application.

Index Terms—PCB inductor, flexible magnetic sheets, optimization of volume, thermal issues, GaN converters.

I. INTRODUCTION

POWER electronics has undergone a strong progression in past decades, thanks to the development of new technologies of passive and active components needed for high frequency power converters. This allows to enhance the power density and the efficiency of power systems and reduce their cost [1], [2]. The increase of the switching frequency of Gallium Nitride (GaN) transistors reduces the values and the volume of the passive components, mainly inductors which take a large volume in converters. This increase in the switching frequency is mainly linked to the reduction of the switching time of the active components. Compared with other components based on Silicon (Si) and Silicon Carbide (SiC), transistors based on GaN offer a lower switching time, thanks to the high electron mobility of Gallium Nitride material, which increases the current density of GaN transistors, and reduces therefore their channel length and parasitic capacitances [3], [4]. However, very fast switching is limited notably by parasitic inductances in the switching mesh, and is associated to possible electromagnetic compatibility (EMC) issues [5], [6]. Thus, power density improvement also relies on the development of magnetic and dielectric materials

that enhances the energy density and the efficiency of inductors and capacitors [7], [8].

Inductors are required in converters for energy storage and filtering [9], [10]. They suffer from a weak energy density compared to capacitors. They are often the largest components in converters ; thus, designers must pay attention to their volume when selecting their inductance value and core shape. PCB inductors are simple to realize, low cost and allow to have planar shapes of small thickness. Several issues appear for the design of these inductors for high-frequency converters like: the choice of the appropriate magnetic material, the resonance frequency, AC copper and magnetic losses that increase with frequency, temperature rise, etc.

Magnetic material allows to improve the energy density of inductors. The Manganese-zinc (ZnMn) and Nickel-zinc (NiZn) ferrites are the most common magnetic materials used for medium and high frequency applications, thanks to their low losses and high relaxation frequency [11].

The capacitive effects due to parasitic capacitance between windings reduce the operating range of inductors in high frequency. The calculation of the stray capacitances of inductors is based on analytical formulas by using some approximations [12], [13], and simulations based on finite element method [14], [15].

Losses produced by inductors represent an important part of converters losses. AC copper losses and magnetic losses become more important in high frequency. Dowell and Ferreira formulas are often used to estimate the AC resistance of inductors needed for AC copper losses calculation in low frequency [16], [17]. In high frequency, the AC resistance calculation is based on simulation tools, because of the difficulty to predict the magnetic flux lines [18]. Magnetic losses due to hysteresis and eddy current are often calculated with Steinmetz formulas [19], [20]. Thermal issues of magnetic materials used for inductors are not often considered in literature [21], [22].

In this paper, a two-layer PCB inductor is considered for high frequency DC-DC converter [23]. The aim of this work is to propose a simple design method based on 2D finite-element method (FEM) that notably links together electromagnetic (EM) and thermal aspects, including geometric optimization as well. Various modeling methods exist, especially for toroidal and planar cores [24]–[26] but seldom for PCB-integrated inductors [27], [28]. While 3D FEM is usually used for non-PCB inductor design, 2D FEM is preferred in this work so as to optimize a PCB-integrated device. Since the considered geometry can be considered near-axisymmetric, 3D FEM can be avoided to save computing time. First, the structure of the PCB inductor and the chosen magnetic sheets will be presented. Second, the algorithm based on the optimization of the

A. Chafi is with University of Lille¹ and University of Sherbrooke² (email: ammar.chafi.etu@univ-lille.fr)

N. Idir and A. Videt are with ¹Univ. Lille, Arts et Metiers Institute of Technology, Centrale Lille, Yncrea Hauts-de-France, ULR 2697 – L2EP, F-59000 Lille, France (email: nadir.idir@univ-lille.fr ; arnaud.videt@univ-lille.fr)

H. Maher is with ²Laboratoire Nanotechnologies Nanosystèmes, CNRS UMI-3463, Institut Interdisciplinaire d'Innovation Technologique, Université de Sherbrooke, Sherbrooke, QC J1K 0A5, Canada (e-mail: hassan.maher@usherbrooke.ca)

inductor volume is executed for many inductance values. The optimal inductance value needed for the converter is chosen from a Losses-Volume curve. The last section is dedicated to the experimental validation of the chosen PCB inductor. The inductor will be realized, characterized and tested with the GaN-based synchronous boost converter in order to evaluate its electrical and thermal characteristics. Simulation results will be compared with experimental data to validate the proposed method.

II. DESIGN METHOD OF THE PCB INDUCTOR

The PCB inductor is designed for a GaN-based synchronous boost converter with these specifications; switching frequency $f = 1$ MHz, power of $P = 100$ W, input voltage $V_i = 48$ V and output voltage $V_o = 100$ V. The inductor structure, the inductance value and the design method must be defined to realize the PCB inductor for converter.

A. Structure of the PCB inductor

The considered geometry of the PCB inductor is shown in Fig. 1a. The windings of spiral form are realized on the two copper layers. This structure is chosen because of the simplicity of its realization compared to toroidal PCB inductor. The advantage of the magnetic sheet is that it can be cut into various shapes of different custom dimensions for PCB inductors, so that the optimal size obtained by the design method presented in this paper can be easily realized. This is not allowed with magnetic cores that have a standardized dimensions and shapes in manufacturer catalogs. Due to the small thickness of magnetic sheets, such inductors are thin and avoid additional height taken on the PCB faces compared with toroidal cores for instance. Fig. 2 shows the complex permeability of three magnetic sheets of different manufacturers; 38M6 from *Fair Rite*, MHLL from *Lairdtech* and IFL10M from *TDK*. Other characteristics like saturation curve $B(H)$ are not provided by manufacturers. The ideal case for the choice of the appropriate magnetic material is to have high initial permeability to increase the energy density of the inductor without magnetic losses that are represented by the secondary permeability $\mu_r''(f)$. The 38M6 is characterized by high initial permeability of $\mu_{r_i} = 230$ up to 5 MHz, and its losses start to increase from 2 MHz. The IFL10M initial permeability is smaller and the magnetic losses are less important compared to 38M6. The MHLL has the advantage that magnetic losses are negligible before 20 MHz. Even though permeability curves are obtained with small-signal excitation, it is assumed that the material power losses can be neglected in the inductor design due to MHLL $\mu_r''(f)$ remaining very small for the first ten significant switching harmonics of a 1-MHz-operated converter. The high relaxation frequency of this material is suitable for inductors designed for megahertz switching power converters. Therefore, the MHLL magnetic sheets is chosen for the realization of the PCB inductor. It should be noted that the primary application of commercially available magnetic sheets is for EM shielding rather than power electronics inductors and their operating temperature range is limited below 100 °C; however manufacturers may eventually increase this limit

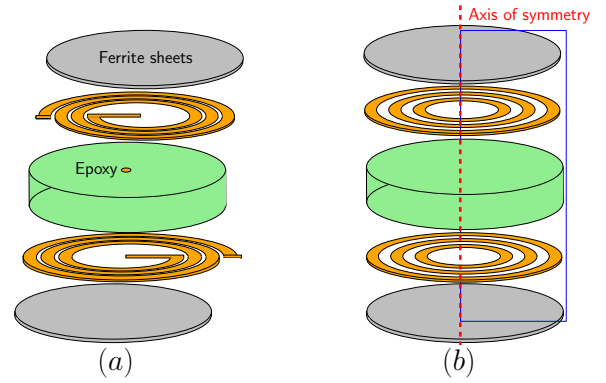


Fig. 1: PCB inductor structure a) circular spiral form (3D) b) concentric circles (2D)

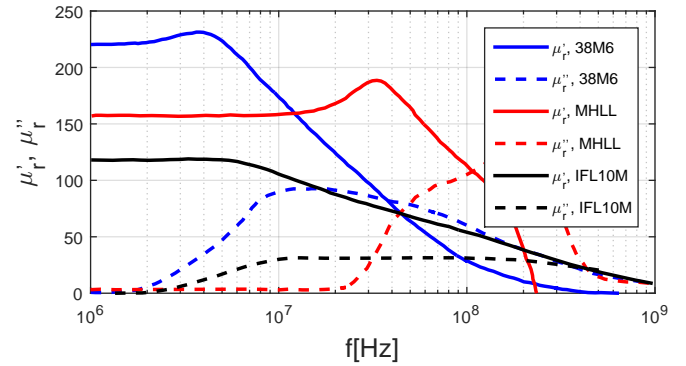


Fig. 2: Complex permeability of magnetic sheets

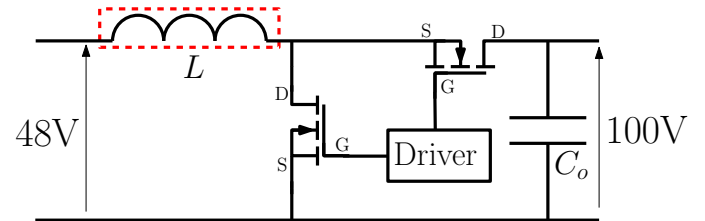


Fig. 3: Boost synchronous converter 1 MHz, 100 W

and provide materials more adapted to HF power electronics applications.

B. Choice of the inductance value

As given in equation 1, the inductor current ripple ΔI_L of the converter shown in Fig. 3 is inversely proportional to the inductance value L for a given duty cycle D , input voltage V_i , and switching frequency f .

$$\Delta I_L = \frac{D \times V_i}{L \times f} \quad (1)$$

Fig. 4 shows the evolution of the current ripple ΔI_L as a function of the inductance value needed for the GaN converter. The inductor current is going negative for inductance values smaller than $L = 6 \mu\text{H}$. Inductors with small inductance values take less volume, but their AC copper losses increase with current ripple. This may cause thermal issues for magnetic

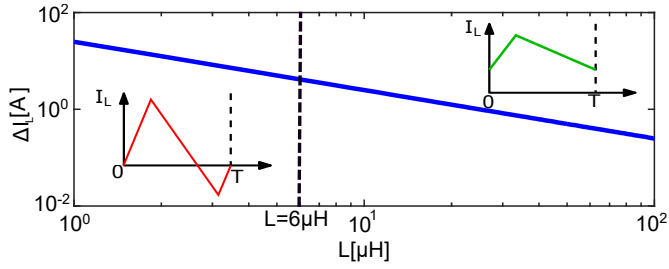


Fig. 4: Inductor current ripple as function of inductance value

sheets of the PCB inductor. So, in this study, the research for the inductance value needed for the converter is done in the interval when the inductor current is positive to reduce AC copper losses and so the temperature rise of the magnetic sheets. It is well known that the volume and DC copper losses are more important for inductors with large inductance value. Also, they suffer from a small resonance frequency that reduces its operating range in high frequency.

C. Calculation tool used for the PCB inductor design

The PCB inductor is designed for 1 MHz converter. The inductance value must be calculated at this frequency. Even though analytical calculations can be done with simple coils [29], they can hardly be applied with the magnetic sheet including large air gaps: the prediction of the magnetic flux path becomes complex especially in high frequency where skin and proximity effects change the current distribution and the magnetic flux path. In this case, FEM simulations are usually needed for magnetic devices analysis [30]. Then, FEMM simulation tool based on finite element method will be used in this work with some hypotheses to design the PCB inductor:

- The spiral form of winding are replaced by circular form in the 2D axisymmetric simulation as shown in Fig. 1b. Spiral form requires 3D simulation tools that are time consuming.
- Small signal design: saturation is not taken into account.
- Magnetic losses are neglected because the imaginary part of the complex permeability μ_r'' of MHL is negligible before 20 MHz.

The magnetic simulation example in Fig. 5 shows how the magnetic sheet captures magnetic field lines and plays an important role on magnetic field around the copper turns, which requires FEM models for accurate analysis. Note that the 2D axisymmetric model is also simplified to a quarter section by considering plane symmetry properties in the two-layer arrangement shown in Fig. 1b.

III. DETERMINATION OF THE GEOMETRICAL PARAMETERS OF THE INDUCTOR

For each inductance value, there is 8 parameters to determine as shown in Fig. 6: the number of turns N , the inner radius r_i , the spacing between tracks s , the width of tracks l , the external distance d_e , the thickness of the magnetic sheets h_m , of copper h , and of Epoxy h_{pcb} . PCB with high thickness

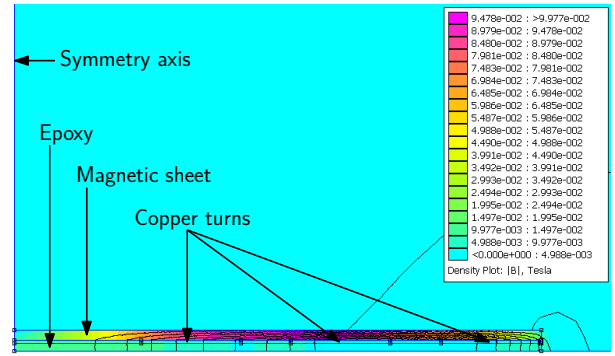


Fig. 5: Flux density plot using FEMM software

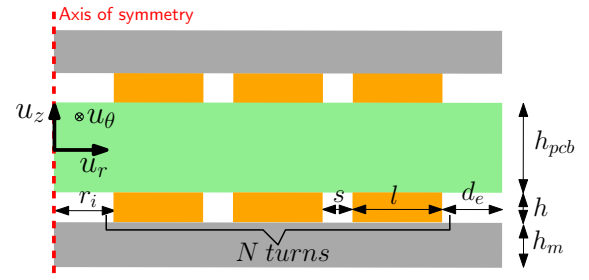


Fig. 6: Geometrical parameters of the PCB inductor

of copper allows to reduce the inductor DC losses. Then, a double copper layers PCB is chosen with $h = 105 \mu\text{m}$ of copper thickness and $h_{pcb} = 1.6 \text{ mm}$ for Epoxy. It is the PCB with highest copper thickness found on the market. In order to increase the energy density of the PCB inductor, the spacing between tracks s is fixed to the minimal distance $s = 0.25 \text{ mm}$ defined by our engraving copper process. An algorithm based on the optimization of the inductor volume is used to determine the other five parameters taking into account thermal issues of the magnetic sheets. Also, a simulation method is proposed to calculate the equivalent stray capacitance of the PCB inductor allowing to determine its resonance frequency. The PCB inductor should keep inductive behavior at the switching frequency of the converter.

A. Optimization algorithm of the inductor volume

The algorithm allowing the determination of the geometrical parameters of the PCB inductor is shown in Fig. 7. It is based on the optimization of the inductor volume using Matlab and FEMM softwares. The spacing between tracks s , the thickness of PCB h_{pcb} and of copper h shown in Fig. 6 are defined as input parameters of this algorithm. The other parameters N , r_i , d_e , and h_m are defined as output parameters. The algorithm is executed for different inductance values from $L = 6 \mu\text{H}$ to $70 \mu\text{H}$, in order to choose the best inductor to meet with the GaN-converter specifications. For each inductance value, the main algorithm is executed for a width of tracks l that varies between $l_0 = 0.5 \text{ mm}$ and $l_{max} = 2 \text{ mm}$ with a step of $\Delta l = 0.5 \text{ mm}$. Discrete numbers like the number of turns N are not computed by the used optimization tool based on Gradient method. Then, an iteration loop is used to

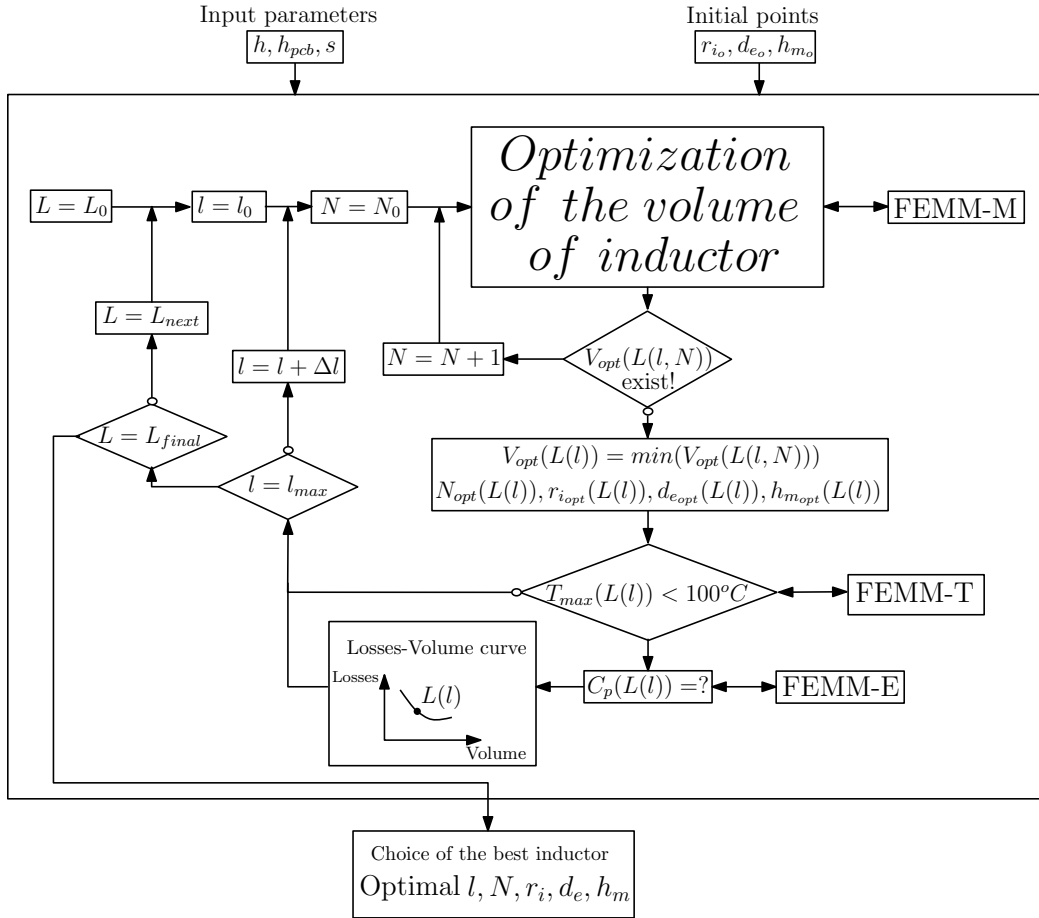


Fig. 7: Flow chart of the inductor volume optimization algorithm

solve this issue. The algorithm calculates the optimal volume $V_{opt}(L(l, N))$ for each number of turns, and it exits from the loop when the computed number of turns gives an inductance value greater than that defined in the constraint. The optimal inductor volume $V_{opt}(L(l))$ is the smallest volume in the vector volume $V_{opt}(L(l, N = N_0 : N_{max}))$. Note that r_{i_o} , d_{e_o} , h_{m_o} in Fig. 7 designate the initial guess required by the optimization procedure for the r_i , d_e , h_m parameters defined in Fig. 6. Likewise, N_0 and l_0 are user-defined initial parameter values that will be subsequently iterated by the proposed algorithm. Different inductance values are tested from L_0 to L_{final} where this range can be determined based on the converter specifications [31] to avoid testing irrelevant inductance values.

Calls from MATLAB to FEMM are initiated at different places in the flowchart depending on the kind of requested FEM analysis: FEMM-M is a short name for magnetic simulations performed both in DC and in AC for the first ten relevant switching harmonics; FEMM-E is a short name for electrostatic simulations that are performed to compute the inductor equivalent capacitance; and FEMM-T relates to thermal simulations detailed in section III-C. Then each FEMM simulation result is sent back to MATLAB in which the optimization itself is implemented.

The maximal temperature of the magnetic sheets will be checked later. If it is lower than the maximum temperature

allowed of 100°C , the equivalent stray capacitance of the inductor will be calculated in order to verify that its resonance frequency is superior than the switching frequency of the converter. Next, the optimized inductor design $L(l)$ for the current track width l will be appended to a Losses-Volume data set for further plotting of the results. Then the algorithm will be executed for the next width of tracks increased by Δl up to the maximal user-defined value l_{max} , where the algorithm will move to the next inductance value L_{next} . The optimization tool stops calculation when the computing inductance is equal to a maximal user-defined value $L_{final} = 70 \mu\text{H}$. User-defined boundaries are just a means of avoiding nonrealistic parameter values so as to provide only relevant information for designers. Thus, the best inductor for the operating of the converter will be eventually chosen from the obtained Losses-Volume curve that will be discussed in section III-D.

B. Calculation of the equivalent stray capacitance

The PCB inductor is designed for 1 MHz converter. Therefore, its resonance frequency must be higher than this switching frequency. For this reason, it is necessary to calculate the equivalent stray capacitance of the inductor. Because of the complexity of analytical calculations, the determination of the equivalent stray capacitance of the inductor is made by electrostatic simulation on FEMM software using the concentric

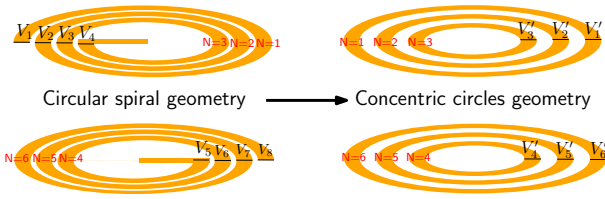


Fig. 8: Approximation used to calculate the stray capacitance

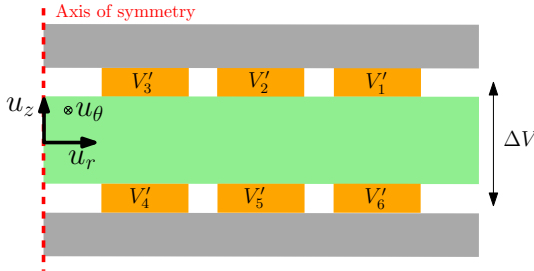


Fig. 9: Electrostatic simulation of the PCB inductor

circles geometry as shown in Fig. 8. Voltages of turns are not varying with u_θ axis as shown in Fig. 9, because of the limitation of the axisymmetric simulation. These voltages are calculated from the root mean square of voltages of turns for the spiral form as given in equation 2 because the variation of the electrostatic energy is proportional to the square voltage. Voltages of spiral turns V_i are calculated from the voltage drops caused by the turns.

$$V'_i = \sqrt{(V_i^2 + V_{i+1}^2)/2} \quad (2)$$

After setting the V_i turns potentials, an electrostatic FEM simulation (FEMM-E call in Fig. 7) is performed to build the electric field map and determine the overall stored electrostatic energy. This energy is linked to the equivalent stray capacitance and the difference of potentials between the first and the last inductor turns, which allows to determine this capacitance value.

C. Calculation of the temperature rise

The maximal operating temperature of the used magnetic sheets is limited to 100 °C. This constraint must be taken into account in the design of the inductor. 3D simulation tools are needed for the thermal simulation of the PCB inductor integrated to the converter. Also, losses of the other components of the converter must be evaluated. For this work, the maximal temperature of the magnetic sheets is calculated by FEMM 2D-axisymmetric simulation neglecting the thermal interaction between the inductor and the other devices of the converter (FEMM-T call in Fig. 7). The half-cross section of the inductor for thermal simulation is shown in Fig. 10. The vertical disposition of the inductor is chosen to facilitate the temperature measurement in the two sides of the inductor and to enhance its cooling.

The coefficient for the natural convection by air is fixed to $h_c = 16 \text{ W}/(\text{m}^2 \text{ K})$. This value is determined from measurements made on another PCB inductor. The thermal simulation

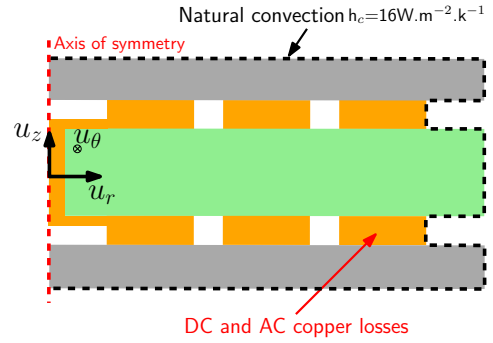


Fig. 10: Thermal simulation of the PCB inductor

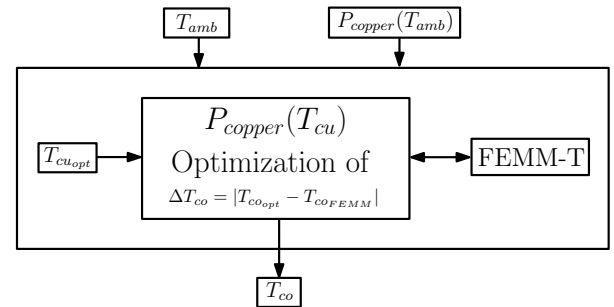


Fig. 11: Algorithm for the calculation of inductor temperature

with FEMM software does not take into account the variation of copper losses with temperature rise due to resistivity change. Then, to avoid this constraint, the algorithm shown in Fig. 11 is used to calculate the maximal temperature of the magnetic sheets. It evaluates the copper temperature difference between that calculated by FEMM software T_{co_FEMM} and that previously obtained by the proposed algorithm T_{co_opt} until convergence to the same value. More specifically, assuming an initial resistivity at 25 °C, copper losses are first calculated and temperatures are determined for each winding turn. Next, the copper resistivity is updated for each turn according to these newly found temperatures, resulting in a updated losses distribution among the turns. Therefore the process is repeated with another evaluation of temperatures based on the new power losses. Iteratively, copper tracks resistivities are updated again and the process is repeated until a fixed point is obtained where temperature stabilizes between two iterations. At this point, the power losses and actual temperature of each turn is obtained, which improves accuracy of the thermal analysis.

It should be noted that, due to the harmonic content of triangular-shaped inductor current quickly decreasing with frequency, speed-up of FEM computation is obtained by considering only the DC component and the first ten harmonics for losses estimation. Notably, the fundamental switching harmonic at 1 MHz is responsible for most AC losses. Even though the AC RMS value is small compared with the DC component, its contribution to losses must not be neglected because of larger AC resistance as will be presented in section IV-A.

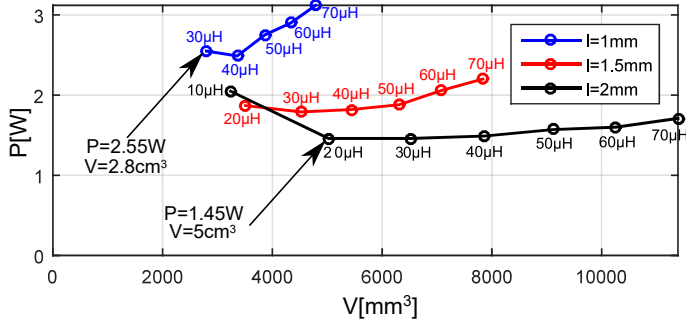


Fig. 12: PCB inductors losses as function of volume

D. Simulation results

When the proposed algorithm from Fig. 7 is executed, the optimal geometry is determined for each inductance value L including the best number of turns N to minimize its volume. Thermal verification is performed in the process to avoid exceeding the specified maximum temperature. Various inductance values are mapped in this way, each one obtained with optimal turns number, which allows proper selection of inductor design based on a losses-volume trade-off curve as presented in Fig. 12. Thus, the algorithm output leaves the final choice for the designer to emphasise efficiency or power density, while each point in Fig. 12 is volume-optimized for a given inductance value. Inductors that not respect the constraint of temperature are not presented in this curve. The objective is to provide a trade-off comparison between losses and volume of inductors, so that designers can select the appropriate inductor realization for their application. It should be noted that in this work, magnetic sheet thickness was constrained by the manufacturer. While a standard 1.6mm PCB thickness has been considered, the method could be applied to smaller values as well; however copper thickness should not be reduced as the losses penalty would be significant. As previously mentioned, the spacing between tracks is kept minimal to reduce total copper length and thereby losses.

In Fig. 12, the minimum of losses $P = 1.45\text{ W}$ corresponds to the $20\text{ }\mu\text{H}$ inductor for a width of tracks $l = 2\text{ mm}$ and a volume $V = 5\text{ cm}^3$. The $30\text{ }\mu\text{H}$ inductor with a width of tracks $l = 1\text{ mm}$ has the minimum volume of $V = 2.8\text{ cm}^3$ with $P = 2.55\text{ W}$ of losses. The 1.1 W of difference between the two inductors losses represents 1.1% of the power of the converter. The $30\text{ }\mu\text{H}$ inductor volume is more smaller compared with the volume of the $20\text{ }\mu\text{H}$ inductor by a factor close to the half. Therefore, because inductors are the largest components in converters and the difference in losses between the two inductors represents 1.1% of the power converter, the $30\text{ }\mu\text{H}$ inductor is chosen and will be used in the converter in the following section.

IV. EXPERIMENTAL VALIDATION

The realized inductor without and with magnetic sheets is shown in Fig. 13. Its external diameter is about 40 mm with a width of tracks $l = 1.5\text{ mm}$ and number of turns $N = 14$. Obviously, the occupied area may be larger than standard off-the-shelf components, as a counterpart of avoiding additional

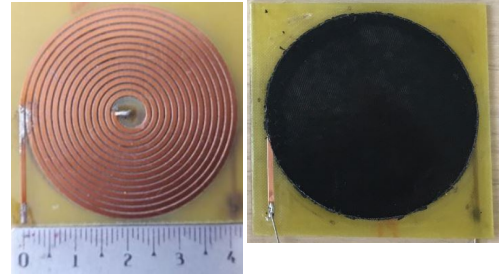


Fig. 13: Realization of the PCB inductor

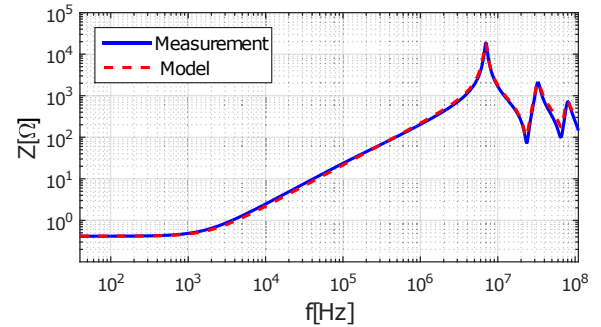


Fig. 14: Measurement of the inductor impedance amplitude

TABLE I: Comparison between simulation and measurement results for the first resonance frequency

	L [μH]	C_p [pF]	R_{dc} [m Ω]
Experimental	32.5	16	0.41
Simulation	31.3	13.79	0.34
Error	4%	14%	17%

height on the PCB faces. Still, the custom-shape magnetic material allows optimized realization according to the algorithm outputs, and applications with different parameters such as switching frequency might result in even better trade-offs using the same proposed method.

This inductor will be characterized and tested with the GaN converter in order to evaluate its electrical and thermal performances. In these tests the converter and inductor are placed in free air without additional air flow, so as to comply with the natural convection conditions considered in section III-C. Forced air flow would require different heat exchange parameters in the simulation setup.

A. Small signal characterization

The measurement of the inductor impedance with impedance analyser (Agilent 4294A, 40Hz-110MHz) is shown in Fig. 14. The first resonance frequency of the realized inductor of 7 MHz is suitable for 1 MHz switching frequency of the GaN converter. Table I shows the comparison between simulation and measurement results for the first resonance frequency. The inductance value is extracted from the inductor measured impedance at 1 MHz . The equivalent stray capacitance linked to the inductor is determined using the RLC model shown in Fig. 15, where R_0 is the DC resistance and the three parallel R, L, C sections resonate around the respective maxima of

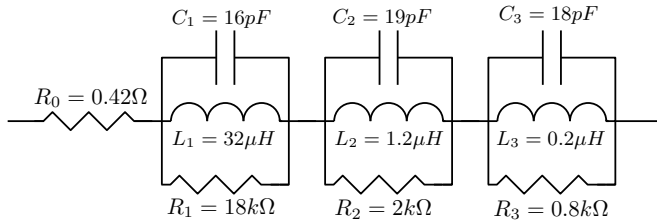


Fig. 15: Modeling of the PCB inductor

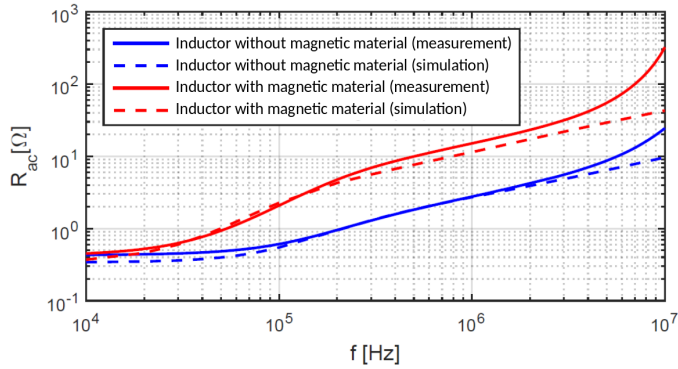


Fig. 16: AC resistance comparison

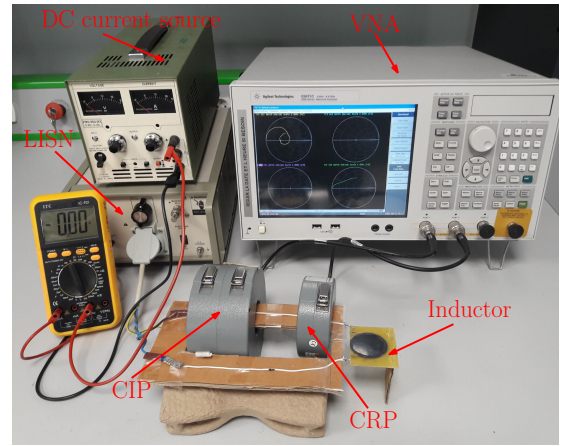
Fig. 14 impedance curve. The component values in Fig. 15 are obtained by fitting over the whole frequency range of the measured inductor impedance. A micro-ohm meter is used for the DC resistance measurement. The difference between measurement and simulation results of Table I may be due to the realization of the PCB that introduces modifications on the inductor dimensions. AC resistance comparison presented in Fig. 16 also shows a good agreement from low frequency to the megahertz range. Notably, both simulations and measurements reveal the magnetic sheets impact modifying the magnetic field and increasing AC resistance by a similar amount.

B. Saturation of the inductor

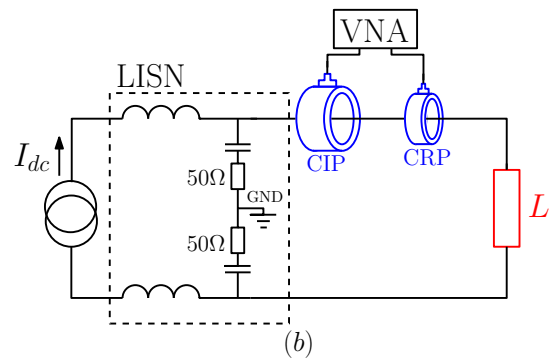
The DC current flowing through the inductor may cause its saturation and reduces its inductance value. To verify this phenomenon, the test bench setup shown in Fig. 17 is used. The characterization method is based on S-parameters named “Multiprobes measurement method” [32], [33]. The inductor impedance \bar{Z}_L is determined using equation 3. Where \bar{Z}_{setup} and \bar{K} are respectively the impedance of the test bench setup and the coefficient of coupling between the setup wire and the current probes. A vector network analyzer (VNA: Agilent E5071C, 9kHz-4.5GHz) is used to measure the S-parameters \bar{S}_{11} and \bar{S}_{21} through two current probes CIP (Current Injection Probe: FCC F-120-3, 10kHz-100MHz) and CRP (Current Reception Probe: FCC F35, 1kHz-100MHz). A DC current source is used for the polarization of the inductor.

$$\bar{Z}_L = \bar{K} \cdot \left(\frac{\bar{S}_{11} + 1}{\bar{S}_{21}} \right) - \bar{Z}_{setup} \quad (3)$$

Fig. 18 shows the variation of the inductance value as a function of the DC current. It decreases from 32 μ H without



(a)



(b)

Fig. 17: a) Test bench setup b) Equivalent model circuit

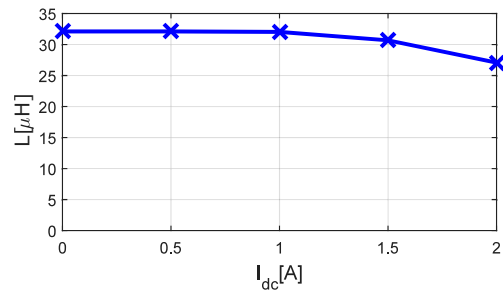


Fig. 18: Inductance value for different DC current

DC current to 27 μ H with 2 A. This decrease is due to the saturation of the magnetic material of the inductor.

C. Inductor tested with the GaN converter

The realized inductor is tested with a GaN Systems converter board where inductor current is monitored by means of a 100-MHz-bandwidth Hall effect current probe (Keysight N2783A) as shown in Fig. 19. The experimental validation of the inductor was made for this operating point; $V_i = 48$ V, $I_i = 2.1$ A, $V_o = 96$ V, and $f = 1$ MHz. The measured inductor current ripple is about $\Delta I_L = 0.9$ A as shown in Fig. 20. It is higher than the theoretically value of 0.83 A, probably because of the saturation of the inductor and the ideal model of converter used to calculate the current ripple (drop voltages are considered nulls for inductor and transistors, also the switching times). Fig. 21 shows the thermal photo

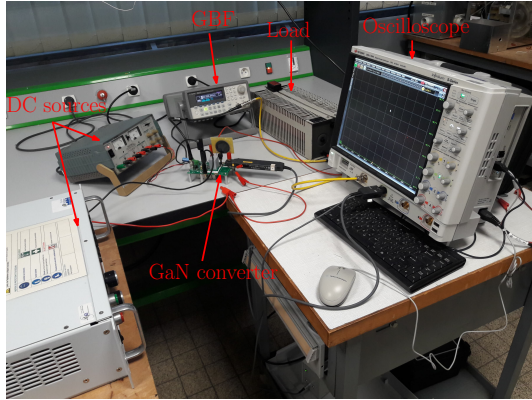


Fig. 19: Experimental setup used to test the PCB inductor with the GaN converter

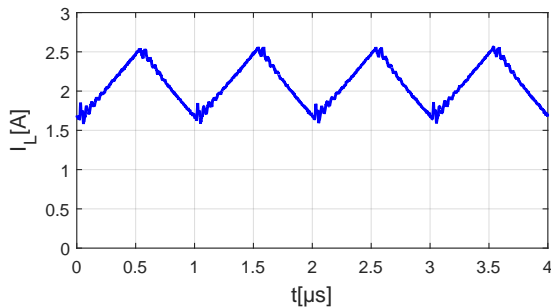


Fig. 20: Current waveform in the inductor

measured with infrared camera of the inductor in operating conditions. The maximal temperature of the magnetic sheets of 92°C is smaller than the authorized maximal temperature of 100°C . The comparison between the profile of the temperature measured and simulated with FEMM is shown in Fig. 22, where the x -axis can be interpreted as the radial distance along a symmetry axis crossing the inductor center in the PCB plane. This profile is extracted from simulated and measured temperature data matrix and shows that the difference in temperature rise between the two profiles is 13% at maximum in the center of the inductor. The origins of this difference can be justified by the error on the DC resistance of the inductor and the saturation of the magnetic sheets which is not taken into account in the design of the inductor. Also, the coefficient for the natural convection by air is defined constant on the two sides of the inductor for the thermal simulation. This coefficient varies with temperature rise which is not uniform on the inductor sides. Also, the coefficient for natural convection by air varies with inductor dimensions and temperature rise.

V. CONCLUSION

In this paper, a design method for PCB inductor is proposed. A high frequency ferrite sheet is used as magnetic material for the inductor in order to enhance its energy density. The inductor is destined to 1 MHz GaN DC/DC converter. Circular spiral shape is chosen for the realization of inductor tracks allowing

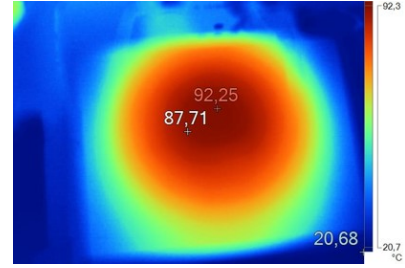


Fig. 21: Measured temperature in the inductor

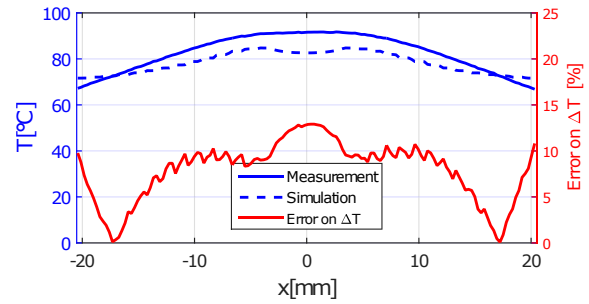


Fig. 22: Temperature profile of measurement and simulation of the inductor

the simulation of the inductor in axisymmetric simulation with FEMM software. Many inductance values can be used for the operating conditions of the converter. The choice of the appropriate value can be made according to several criteria like losses, volume, etc. The design of the PCB inductor is based on finite element method simulation by FEMM software because of the complexity of analytical models. The determination of the different geometrical parameters of the PCB inductor is based on an optimization algorithm of the inductor volume for a given inductance value. The thermal constraint of the magnetic sheets is taken into account in the algorithm. Also, a simulation method is proposed to calculate the equivalent stray capacitance in order to evaluate its resonance frequency that must be higher than the switching frequency of the converter. The inductance value needed for the converter is chosen from a Losses-Volume curve of inductors that respect the constraint of maximum temperature.

The chosen inductor was realized and characterized in small signal. The error between simulation and experimental results is due mainly to the realization of the inductor. The inductor is thereafter tested with the GaN converter in order to evaluate its electrical and thermal performances. The difference between the simulated and the measured temperature profiles is produced mainly by error on the DC resistance of the inductor and the definition of the coefficient for natural convection by air. Thus, the proposed method allows optimal design of high-frequency custom-shape PCB integrated inductors by means of flexible magnetic sheets, with the advantage of 2D FEM that takes into account both electromagnetic and thermal aspects with satisfactory speed and accuracy due to solving axisymmetric equivalent problem.

On the other hand, even though FEMM-MATLAB communication benefits from existing programming interfaces

(API), frequent data exchange between the two softwares might penalize the total speed of the optimization procedure. Also, the realized inductor has small thickness and larger area compared with standard components, which depends on switching frequency and inductor construction. Thus, perspectives of this work include the reduction of inductor volume using other structures such as multilayer PCB windings and the design of inductors taking into account saturation issues of the magnetic sheets for multi-megahertz power converters. Compared with more conventional inductors designs, the full covering of PCB inductor windings by magnetic sheets may provide additional shielding effect, that could also be a subject of future research focusing on radiated performance.

VI. ACKNOWLEDGMENT

This work has been achieved within the framework of CE2I project (Convertisseur d'Énergie Intégré Intelligent). CE2I is co-financed by European Union with the financial support of European Regional Development Fund (ERDF), French state and the French Region of Hauts-de-France

REFERENCES

- [1] J. A. Anderson, E. J. Hanak, L. Schrittwieser, M. Guacci, J. W. Kolar, and G. Deboy, "All-silicon 99.35seven-level hybrid neutral point clamped/flying capacitor inverter," *CPSS Transactions on Power Electronics and Applications*, vol. 4, no. 1, pp. 50–61, March 2019.
- [2] L. Schrittwieser, M. Leibl, and J. W. Kolar, "99three-phase matrix-type dab buck-boost pfc rectifier," *IEEE Transactions on Power Electronics*, pp. 1–1, 2019.
- [3] J. Millan, P. Godignon, X. Perpin, A. Perez-Tomas, and J. Rebollo, "A survey of wide bandgap power semiconductor devices," *IEEE Transactions on Power Electronics*, vol. 29, no. 5, pp. 2155–2163, May 2014.
- [4] S. Ji, D. Reusch, and F. C. Lee, "High-frequency high power density 3-d integrated gallium-nitride-based point of load module design," *IEEE Transactions on Power Electronics*, vol. 28, no. 9, pp. 4216–4226, Sep. 2013.
- [5] H. Nie, Y. Bai, Q. Cheng, and M. J. Scott, "Evaluation of conducted EMI in GaN and Si based isolated dc/dc converters," in *2019 IEEE 7th Workshop on Wide Bandgap Power Devices and Applications (WiPDA)*, 2019, pp. 251–254.
- [6] D. Han, S. Li, W. Lee, W. Choi, and B. Sarlioglu, "Trade-off between switching loss and common mode EMI generation of GaN devices-analysis and solution," in *2017 IEEE Applied Power Electronics Conference and Exposition (APEC)*, 2017, pp. 843–847.
- [7] Y. Su, Q. Li, and F. C. Lee, "Design and evaluation of a high-frequency LTCC inductor substrate for a three-dimensional integrated dc/dc converter," *IEEE Transactions on Power Electronics*, vol. 28, no. 9, pp. 4354–4364, Sep. 2013.
- [8] O. Goualard, N. Videau, T. Meynard, T. B. Doan, T. Lebey, V. Bley, and E. Sarraute, "Integrated dc-dc based-gan converter with screen printed capacitors allowing double side cooling," in *IECON 2014 - 40th Annual Conference of the IEEE Industrial Electronics Society*, Oct 2014, pp. 1549–1555.
- [9] B. Zaidi, A. Videt, and N. Idir, "Optimization method of CM inductor volume taking into account the magnetic core saturation issues," *IEEE Transactions on Power Electronics*, vol. 34, no. 5, pp. 4279–4291, May 2019.
- [10] C. Cuellar, A. Benabou, and N. Idir, "Characterization and modeling of hysteresis for magnetic materials used in EMI filters of power converters," *IEEE Transactions on Power Electronics*, vol. 29, no. 9, pp. 4911–4920, Sep. 2014.
- [11] M. S. Rylko, K. J. Hartnett, J. G. Hayes, and M. G. Egan, "Magnetic material selection for high power high frequency inductors in dc-dc converters," in *2009 Twenty-Fourth Annual IEEE Applied Power Electronics Conference and Exposition*, Feb 2009, pp. 2043–2049.
- [12] M. Kovacic, Z. Hanic, S. Stipetic, S. Krishnamurthy, and D. Zarko, "Analytical wideband model of a common-mode choke," *IEEE Transactions on Power Electronics*, vol. 27, no. 7, pp. 3173–3185, July 2012.
- [13] A. Massarini and M. K. Kazimierczuk, "Self-capacitance of inductors," *IEEE Transactions on Power Electronics*, vol. 12, no. 4, pp. 671–676, July 1997.
- [14] Y. Liu, K. Y. See, J. Lai, K. J. Tseng, Y. Liu, C. F. Tong, A. Nawawi, S. Yin, A. Sakanova, R. Simanjorang, C. J. Gajanayake, and A. K. Gupta, "FEM modelling of three-phase common mode choke for performance evaluation," in *2016 Asia-Pacific International Symposium on Electromagnetic Compatibility (APEMC)*, vol. 01, May 2016, pp. 96–99.
- [15] Qin Yu and T. W. Holmes, "A study on stray capacitance modeling of inductors by using the finite element method," *IEEE Transactions on Electromagnetic Compatibility*, vol. 43, no. 1, pp. 88–93, Feb 2001.
- [16] P. L. Dowell, "Effects of eddy currents in transformer windings," *Proceedings of the Institution of Electrical Engineers*, vol. 113, no. 8, pp. 1387–1394, August 1966.
- [17] J. A. Ferreira, "Appropriate modelling of conductive losses in the design of magnetic components," in *21st Annual IEEE Conference on Power Electronics Specialists*, 1990, pp. 780–785.
- [18] A. Pereira, F. Sixdenier, M. A. Raulet, B. Lefebvre, and N. Burais, "Comparison between numerical and analytical methods of ac resistance evaluation for medium-frequency transformers: Validation on a prototype and thermal impact analysis," *Canadian Journal of Electrical and Computer Engineering*, vol. 40, no. 2, pp. 101–109, Spring 2017.
- [19] C. P. Steinmetz, "On the law of hysteresis," *Transactions of the American Institute of Electrical Engineers*, vol. IX, no. 1, pp. 1–64, Jan 1892.
- [20] Jinjun Liu, T. G. Wilson, R. C. Wong, R. Wunderlich, and F. C. Lee, "A method for inductor core loss estimation in power factor correction applications," in *APEC. Seventeenth Annual IEEE Applied Power Electronics Conference and Exposition (Cat. No.02CH37335)*, vol. 1, March 2002, pp. 439–445 vol.1.
- [21] R. Bakri, J. S. N. Teu, X. Margueron, P. Le Moigne, and N. Idir, "Planar transformer equivalent thermal resistance variation with ambient temperature and power losses," in *2016 18th European Conference on Power Electronics and Applications (EPE'16 ECCE Europe)*, Sep. 2016, pp. 1–9.
- [22] M. Delhommeais, J. Schanen, F. Wurtz, C. Rigaud, S. Chardon, and S. Vighetti, "Thermal model of litz wire toroidal inductor based on experimental measurements," in *2018 IEEE Applied Power Electronics Conference and Exposition (APEC)*, March 2018, pp. 2658–2665.
- [23] Y. Dou, Z. Ouyang, P. Thummala, and M. A. E. Andersen, "PCB embedded inductor for high-frequency ZVS SEPIC converter," in *2018 IEEE Applied Power Electronics Conference and Exposition (APEC)*, 2018, pp. 98–104.
- [24] Q. Li, Y. Su, M. Mu, F. C. Lee, and D. Gilham, "Modeling of planar inductors with non-uniform flux distribution and non-linear permeability for high-density integration," in *2012 Twenty-Seventh Annual IEEE Applied Power Electronics Conference and Exposition (APEC)*, 2012, pp. 1002–1009.
- [25] A. Camarda, E. Macrelli, A. Romani, and M. Tartagni, "Design optimization of integrated magnetic core inductors," *IEEE Transactions on Magnetics*, vol. 51, no. 7, pp. 1–10, 2015.
- [26] C. Ropoteanu, P. Svasta, and C. Ionescu, "A comparative simulation analysis of toroid and planar magnetic cores near MHz region," in *2017 IEEE 23rd International Symposium for Design and Technology in Electronic Packaging (SIITME)*, 2017, pp. 259–262.
- [27] S. C. Tang, S. Y. R. Hui, and H. S. . Chung, "A low-profile power converter using printed-circuit board (PCB) power transformer with ferrite polymer composite," *IEEE Transactions on Power Electronics*, vol. 16, no. 4, pp. 493–498, 2001.
- [28] Y. Pascal, M. Petit, D. Labrousse, and F. Costa, "Study of a topology of low-loss magnetic component for PCB-embedding," in *2018 7th Electronic System-Integration Technology Conference (ESTC)*, 2018, pp. 1–7.
- [29] S. S. Mohan, M. del Mar Hershenson, S. P. Boyd, and T. H. Lee, "Simple accurate expressions for planar spiral inductances," *IEEE Journal of Solid-State Circuits*, vol. 34, no. 10, pp. 1419–1424, 1999.
- [30] A. Reatti and M. K. Kazimierczuk, "Comparison of various methods for calculating the ac resistance of inductors," *IEEE Transactions on Magnetics*, vol. 38, no. 3, pp. 1512–1518, 2002.
- [31] He Li-gao and Wu Jian, "Selection of the current ripple ratio of converters and optimal design of output inductor," in *2010 5th IEEE Conference on Industrial Electronics and Applications*, 2010, pp. 1163–1167.
- [32] V. Tarateeraseth, B. Hu, K. Y. See, and F. G. Canavero, "Accurate extraction of noise source impedance of an SMPS under operating conditions," *IEEE Transactions on Power Electronics*, vol. 25, no. 1, pp. 111–117, Jan 2010.

- [33] K. Li, A. Videt, and N. Idir, "Multiprobe measurement method for voltage-dependent capacitances of power semiconductor devices in high voltage," *IEEE Transactions on Power Electronics*, vol. 28, no. 11, pp. 5414–5422, Nov 2013.